Communications In Catalysis
Vol. 3, No. 1, 2026, pp. 57-72
DOI: 10.22049/cic.2026.32234.1046
Azarbaijan Shahid Madani University

Localized Microwave Heating in Alkaline Water Electrolysis: Electrode-Current Redistribution, Thermal Controls, and Energy Penalties

Shahram Hosseinzadeh[1], * and Zohreh Shaghaghi[2]

[1] Department of Electrical Engineering, Azarbaijan Shahid Madani University, Tabriz, Iran
[2] Department of Chemistry, Faculty of Basic Sciences, Azarbaijan Shahid Madani University, Tabriz, Iran

Email: s.hosseinzadeh@azaruniv.ac.ir

Received: 2026-05-22, Accepted: 2026-06-10

Abstract

A reduced electromagnetic–electrochemical model of microwave-assisted alkaline water electrolysis was evaluated with matched zero-RF and 2-W numerical controls to distinguish electrolyte-transport effects from intrinsic electrode catalysis and to quantify external-energy penalties. A one-dimensional 2.45-GHz microwave solver was coupled to two-dimensional stationary thermal, charge and reduced hydroxide transport, with illustrative nickel-electrode Butler–Volmer laws. In the 1 cm^3, 1 mol L^{-1} KOH reference cell at 2 V, hydrogen production increased from 9.84609 to 9.94742 mmol h^{-1} between zero and 3 W RF input, while assumed-equipment higher-heating-value efficiency fell from 72.58% to 13.85%. Nine matched 0/2-W comparisons using identical numerical mesh settings found relative increases of 0.763, 0.697 and 0.622% at KOH concentrations of 0.5, 1 and 2 mol L^{-1}; 0.300–0.975% across 1.8–2.2 V; and 0.547–0.829% when both assumed HER/OER exchange-current coefficients were scaled by 0.5–2. A separate RF-power screen remained within the solvent-dielectric temperature range through 3.5 W but exceeded it at 4 W.

Keywords: alkaline water electrolysis, microwave heating, electrode polarization, electrothermal coupling

1. Introduction

Hydrogen produced by water electrolysis is an important route for coupling low-carbon electricity to chemical manufacturing, energy storage, and industrial hydrogen supply. Among the available technologies, alkaline water electrolysis has attracted sustained interest because of its technological maturity and the possibility of using comparatively abundant electrode materials. Its wider implementation, however, depends on improving the electrical energy required per unit of hydrogen, maintaining stable operation at practically relevant current densities, and controlling the coupled electrochemical and thermal behavior of the cell. These requirements have been emphasized in experimental studies, technology assessments, and multiphysics models of water electrolyzers [1-14].

Several interacting limitations prevent these objectives from being achieved simultaneously. Ohmic losses depend on the concentration- and temperature-dependent ionic conductivity of the electrolyte, whereas activation losses depend on the kinetics and surface condition of the hydrogen- and oxygen-evolution electrodes. The electrolyte also possesses a frequency-dependent dielectric response, which must be distinguished from its direct-current conductivity when electromagnetic heating is considered. Although established conductivity correlations and dielectric measurements provide useful starting points, pure-water microwave properties cannot be assumed to represent concentrated KOH solutions [15- 18]. Electrode polarization, catalytic activity, and durability introduce further uncertainties, particularly when nominal kinetic parameters are transferred between different nickel surfaces or operating conditions [19- 26]. Studies of chemically distinct electrocatalysts also demonstrate the sensitivity of reaction performance to interfacial composition and surface state, rather than to heating alone [27-31]. At appreciable gas-evolution rates, bubble coverage, evolving electrolyte resistance, species transport, and heat removal introduce additional coupled limitations [32- 37].

Microwave assistance has been proposed as a means of supplying heat directly to a responsive medium instead of relying exclusively on heat transfer from external surfaces. In alkaline electrolysis, appropriately controlled microwave absorption could modify local electrolyte temperature, ionic conductivity, transport, and the distribution of current between the electrodes. If the electrode interfaces are also heated, temperature-dependent reaction kinetics could contribute to the response. These possible benefits must nevertheless be weighed against spatial hot spots, gas-evolution effects, microwave coupling losses, and the electricity consumed by the microwave source. Moreover, an increase in hydrogen production under irradiation does not, by itself, demonstrate a nonthermal catalytic mechanism or improved system-level efficiency. Reports of microwave-assisted hydrogen generation include ceria-based redox reactions and other processes that differ from DC-biased liquid alkaline electrolysis [38- 41]. An experimental study involving nickel electrodes and 6 mol L^{-1} KOH provides more directly relevant electrolysis context, although its conditions do not calibrate the reduced cell studied here [42].

The present work examines how spatially nonuniform microwave heating modifies the predicted electrochemical response of a simplified alkaline cell. Temperature-dependent electromagnetic absorption is coupled to stationary heat transfer, electrolyte charge transport, and illustrative electrode kinetics. Microwave heating is compared with conventional-heating

controls, while matched zero-RF and 2-W cases are used to evaluate the influence of KOH concentration, applied voltage, and assumed electrode kinetic parameters. Geometry-dependent behavior, hydrogen-production changes, and the external-energy penalty are also assessed. The interpretation is deliberately restricted to thermal and transport effects represented by the governing equations. In particular, the fixed-temperature electrode boundaries and uncalibrated dielectric and kinetic properties prevent claims of intrinsic microwave-induced catalysis or quantitative device-level performance.

The remainder of the paper is organized as follows. The electrochemical formulation and material assumptions are presented first, followed by the microwave-to-heat coupling and energy-accounting approach. The computational configurations, conventional-heating controls, and numerical verification procedures are then described. The results are discussed in terms of local current redistribution, hydrogen production, and energy efficiency, followed by matched electrochemical parameter sensitivities and the screened microwave-power study. The implications of extending microwave power beyond the present constitutive and thermal limits are considered before the remaining validation requirements and principal conclusions are presented.

2. Electrochemical formulation and constitutive assumptions

The distinction between bulk electrolyte transport and interfacial chemical kinetics is essential when a thermal field is spatially nonuniform. The electrolyte temperature controls the conductivity and migration field, while the electrode-face temperature controls the Arrhenius factors in the selected reaction-flux laws. This distinction enables a transparent interpretation of the present boundary conditions.

The cathode and anode are represented by nominal nickel-based electrode-kinetic boundary conditions for the hydrogen evolution reaction (HER) and oxygen evolution reaction (OER), respectively. Nickel is adopted as an illustrative material class for both electrodes rather than as an experimentally characterized electrode pair. The model does not resolve a particular nickel alloy, coating, surface morphology or catalyst loading, nor does it solve heat conduction inside the metallic electrodes. In alkaline electrolyte, the corresponding cathodic and anodic half-reactions are

$$2\mathrm{H_2O} + 2e^- \rightarrow \mathrm{H_2} + 2\mathrm{OH^-}, \quad (1)$$

$$4\mathrm{OH^-} \rightarrow \mathrm{O_2} + 2\mathrm{H_2O} + 4e^-. \quad (2)$$

For a prescribed 2-V metal-to-metal DC potential difference, the modeled electrolyte potential ϕ satisfies

$$\nabla \cdot [\kappa(T,h)\nabla\phi] = 0, \quad \kappa(T,h) = \sigma_{\mathrm{KOH}}(T)\max[0.2, 1 + 0.05(h-1)], \quad (3)$$

where $h = c_{\mathrm{OH^-}}/c_{\mathrm{bulk}}$ is a reduced hydroxide concentration. The electrical-current and hydroxide boundary fluxes use illustrative symmetric Butler–Volmer expressions, with positive reaction-current magnitudes,

$$j_{\mathrm{HER}} = 2j_{0,\mathrm{H}}(T)\sinh\left(\frac{F\phi}{2RT}\right), \quad (4)$$

$$j_{\mathrm{OER}} = 2j_{0,\mathrm{O}}(T)\sqrt{\max(0.05, h)}\,\sinh\left(\frac{F[V_{\mathrm{app}} - \phi - E_{\mathrm{rev}}(T)]}{2RT}\right). \quad (5)$$

The nominal exchange-current densities at $T_0 = 298.15$ K were 5 and 0.5 A m^{-2} for HER and OER, with activation energies of 25 and 35 kJ mol^{-1} in

$$j_{0,k}(T) = j_{0,k}(T_0)\exp\left[\frac{E_{a,k}}{R}\left(\frac{1}{T_0} - \frac{1}{T}\right)\right], \quad E_{\mathrm{rev}}(T) = 1.229 - 0.0009(T - T_0)\ \mathrm{V}. \quad (6)$$

These parameters were prescribed rather than fitted to polarization measurements on actual nickel cathodes and anodes. The HER and OER exchange-current densities are therefore model inputs, not experimentally established properties of a specific electrode

assembly. The electrode model also omits explicit temperature-dependent activities and detailed reaction mechanisms. The reduced hydroxide flux is represented by

$$\nabla \cdot \mathbf{\Gamma}_h = \lambda_{\mathrm{mix}}(1-h), \qquad \mathbf{\Gamma}_h = -D_{\mathrm{OH}}(T)\nabla h + \frac{D_{\mathrm{OH}}(T)F}{RT} h \nabla \phi, \tag{7}$$

with $\lambda_{\mathrm{mix}} = 1\ \mathrm{s^{-1}}$ and $D_{\mathrm{OH}}(T_0) = 5 \times 10^{-9}\ \mathrm{m^2\ s^{-1}}$. The implemented temperature- and molarity-dependent KOH conductivity expression, in S cm^{-1}, is

$$\sigma_{\mathrm{KOH}} = -2.041M - 0.0028M^2 + 0.005332MT + 207.2\frac{M}{T} + 0.001043M^3 - 3 \times 10^{-7}M^2T^2, \tag{8}$$

where M is expressed in mol L^{-1} and T in kelvin; multiplication by 100 gives S m^{-1}. At 1 mol L^{-1} and 298.15 K the implementation gives approximately 21.526 S m^{-1} [1, 15].

The two electrode surfaces were prescribed at $T = T_0$, while the other reduced-domain edges were thermally insulated. This has a decisive chemical consequence, the electrode-surface Arrhenius factors $j_{0,k}(T)/j_{0,k}(T_0)$ equal unity throughout these runs. Although the bulk electrolyte becomes hotter, these simulations do not demonstrate a direct thermal activation of the interfacial rate constants. Changes in current reflect the coupled electrolyte potential, conductivity, and reduced transport response with interfacial overpotential redistribution.

3. Microwave-to-heat coupling and energy accounting

The electrolyte in the reference configuration was modeled as a 2-mm electrode gap, 20-mm RF propagation length, and 25-mm effective extrusion width, giving a volume of 1 cm^3 and electrode area $A_e = 5 \times 10^{-4}\ \mathrm{m^2}$ per face. A reduced one-dimensional electromagnetic field $E(z)$ obeyed

$$\frac{d^2E}{dz^2} + k^2(T,z)E = 0, \qquad k^2 = \omega^2\mu_0\epsilon_0\epsilon^*_{\mathrm{eff}}(T), \tag{9}$$

$$\epsilon^*_{\mathrm{eff}}(T) = \epsilon_\infty + \frac{\epsilon_s(T)-\epsilon_\infty}{1+i\omega\tau(T)} - i\frac{\sigma_{\mathrm{KOH}}(T)}{\omega\epsilon_0}, \tag{10}$$

using the $e^{i\omega t}$ convention at $f = 2.45$ GHz. The dielectric-relaxation term describes pure water, whereas the ionic conduction contribution is calculated separately. This approximation neglects the influence of KOH concentration on the solvent relaxation parameters. The local RF heat source is

$$q_{\mathrm{RF}}(z) = \frac{|E(z)|^2}{2}[\omega\epsilon_0\epsilon_D''(T) + \sigma_{\mathrm{KOH}}(T)]. \tag{11}$$

Net delivered power was defined from the actual time-averaged inlet Poynting flux rather than from the square of a voltage-reflection coefficient in a lossy medium. The field was renormalized to a 1-W net-inlet reference and the heat source scaled to each stated power. Thus the power label is not a microwave oven's nameplate setting or the gross incident power at a real applicator port.

The stationary heat equation is

$$-\nabla \cdot (k_T \nabla T) = q_{\mathrm{RF}} + \kappa(T,h)|\nabla\phi|^2, \qquad k_T = 0.6\ \mathrm{W\,m^{-1}\,K^{-1}}, \tag{12}$$

with temperature-dependent dielectric and ionic response updated iteratively until the stationary RF and thermal states were consistent. Equation (12) includes bulk Joule heat but does not explicitly model electrode activation/reaction heat, real electrode thermal mass, convective cooling, gas evolution or latent heat. Therefore its predicted peaks must not be extrapolated to phase-changing operation.

The hydrogen-production rate was obtained from Faraday's law using an assumed constant Faradaic efficiency of $\eta_F = 0.98$. Here I_{cath} is the total cathodic current and F is Faraday's constant. Two electrons are required per hydrogen molecule, giving

$$\dot{n}_{\mathrm{H_2}} = \frac{\eta_F I_{\mathrm{cath}}}{2F}, \qquad P_{\mathrm{DC}} = V_{\mathrm{app}} I_{\mathrm{cath}}, \tag{13}$$

where V_{app} is the applied cell voltage and P_{DC} is the electrical power supplied to the electrodes. The 98% Faradaic efficiency is prescribed rather than obtained from a gas-purity or crossover calculation. The overall energy-conversion metric is the hydrogen higher-heating-value efficiency, η_{HHV}, defined as the chemical energy rate of the produced hydrogen divided by the total modeled electrical input. The higher heating value includes the heat released when hydrogen is fully oxidized and the product water is condensed; the adopted molar value is $\Delta H_{\mathrm{HHV}} = 285830$ J mol^{-1}. Expressed as a percentage, the illustrative system efficiency is

$$\eta_{\mathrm{HHV}} = 100\,\frac{\dot{n}_{\mathrm{H_2}}\Delta H_{\mathrm{HHV}}}{P_{\mathrm{DC}}+P_{\mathrm{ext}}}, \qquad P_{\mathrm{ext}} = \begin{cases} P_{\mathrm{RF},net}/0.65, & \text{microwave,} \\ P_{\mathrm{heater}}/1.00, & \text{idealized heater.} \end{cases} \tag{14}$$

Here P_{ext} denotes the electrical input attributed to external heating. For the microwave cases, $P_{\mathrm{RF},net}$ is the net electromagnetic power entering the reduced electrolyte domain, rather than the nameplate power of a microwave oven. The denominator consequently accounts for the DC cell input and an assumed microwave-system electrical overhead. The 65% microwave factor was selected as a representative upper-range effective conversion efficiency for a 2.45-GHz magnetron-based heating arrangement. Published assessments have reported efficiencies of approximately 50–65% for microwave-processing systems, depending on the generator, power supply and coupling conditions [43]. Its use here presumes favorable delivery from electrical supply to the modeled net RF inlet and does not constitute a measured wall-plug efficiency or an independently resolved applicator loss.

The conventional-heating control was assigned 100% electricity-to-useful-heat conversion as an idealized upper-bound benchmark, consistent with the near-complete electrical-to-thermal conversion of resistance heating [44]. This assumption neglects losses between a practical heater and the electrolyte and should not be interpreted as 100% electrolysis-system efficiency. Both equipment efficiencies are specified inputs, not experimental results. Pumping, cooling, control electronics, water handling and other auxiliary electrical loads are excluded; accordingly, η_{HHV} is an illustrative system-level energy metric rather than a verified device efficiency.

4. Computational cases, thermal controls and verification

Two conventional-heating controls were evaluated using the same electrochemical equations. In the first control, spatially uniform volumetric heating was adjusted to match the mean electrolyte temperature obtained under microwave irradiation. In the second control, a prescribed volumetric heat source reproduced the spatial distribution of microwave energy deposition. Because the latter control employed an identical heat-source profile, its agreement with the microwave case primarily served as a numerical consistency check.

In addition to the 1 cm³ reference cell A, case B doubled only the extrusion width, case C reduced all three dimensions to 75% at matched net RF power density, and case D used the geometry of C at increased power density to match the nominal reference thermal-source group. These are four cases but only two independently resolved two-dimensional geometries, changing width alone is an analytic scaling operation in this reduced formulation. To assess similarity, the key model groups include

$$\Pi_{\mathrm{RF}} = \frac{(P_{\mathrm{abs}}/V)d^2}{k_T \Delta T_{\mathrm{ref}}}, \qquad \Lambda = 2|\mathrm{Im}\,k(T_0)|L, \qquad \gamma = d/L, \quad \Delta T_{\mathrm{ref}} = 35\ \mathrm{K}. \tag{15}$$

Similar mean absorbed power density alone does not preserve the heat-source shape, electrode kinetic ratios, hydroxide replenishment number or attenuation length.

Thirty-six stationary solutions were evaluated across the four geometrical configurations and three heating conditions. Numerical discretization sensitivity was additionally examined at 3 W for the reference cell using four progressively coarser meshes. The corresponding hydrogen-production rates were 9.94506, 9.94742, 9.95070 and 9.95388 mmol h^{-1}. The second-finest discretization differed from the finest result by 0.0237%. The maximum heat-balance residual across these discretizations was approximately 1.76%, indicating that more stringent thermal conservation checks remain desirable. Further calculations comprised a one-factor-at-a-time electrochemical sensitivity study, a seven-point microwave-power sweep and independent reference-condition checks. All runs were assessed for numerical convergence, microwave power balance and the applicable temperature range. These checks establish numerical consistency under the stated assumptions but do not independently validate electrode kinetics or the concentration-dependent microwave dielectric response of KOH.

5. Results and chemical interpretation

The results are interpreted primarily in terms of electrochemical transport, electrode-current distribution and energy demand. Spatially resolved quantities were obtained from the calculated temperature and potential fields under the same physical assumptions as the integral performance metrics.

Table 1 summarizes the independently computed reference cases. The assumed-equipment η_{HHV} decreases from 72.579% at zero RF to 18.916% at 2 W and 13.847% at 3 W, even though the corresponding hydrogen-production rates increase from 9.84609 to 9.91467 and 9.94742 mmol h^{-1}. The zero-RF case still consumes DC power because the electrodes remain biased at 2 V. Additional microwave electricity therefore raises the total input much faster than the chemical energy output, reducing the calculated system-level efficiency despite the modest hydrogen-rate gain. At 3 W, the volume-averaged temperature increased by only 1.69 K relative to the zero-RF value of 298.18 K, whereas the maximum local temperature reached 325.48 K. The mean temperature characterizes the overall thermal response of the electrolyte, while the maximum temperature provides a criterion for assessing the validity of local material properties and phase assumptions. This pronounced spatial temperature variation arises from the strong microwave attenuation predicted by the adopted lossy-medium model. The reference attenuation number was approximately 15.02 over a propagation distance of 20 mm, corresponding to a uniform-property intensity attenuation length of approximately 1.33 mm.

Table 1: Predicted electrothermal response of the 1 cm^3 reference cell at 2 V. RF power denotes net power delivered into the reduced model.

$P_{RF,net}$ (W)	$\bar{T}$ (K)	T_{max} (K)	$\bar{j}$ (A m^{-2})	$\dot{n}_{H_2}$ (mmol h^{-1})	η_{HHV} (%)
0	298.179	298.195	1077.101	9.84609	72.579
2	299.304	315.900	1084.603	9.91467	18.916
3	299.869	325.477	1088.186	9.94742	13.847

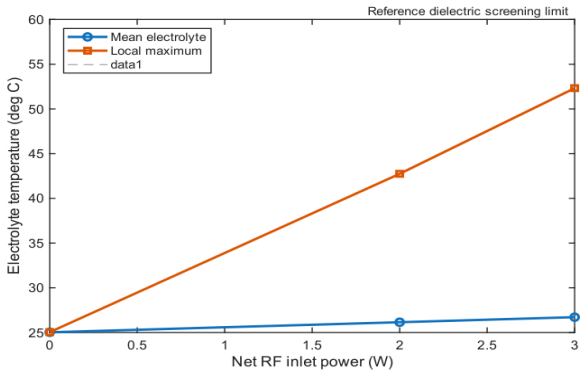

Figure 1: Mean and maximum electrolyte temperatures in the reference cell. The dashed line marks the 333.15-K validity-screening limit of the solvent-relaxation representation.

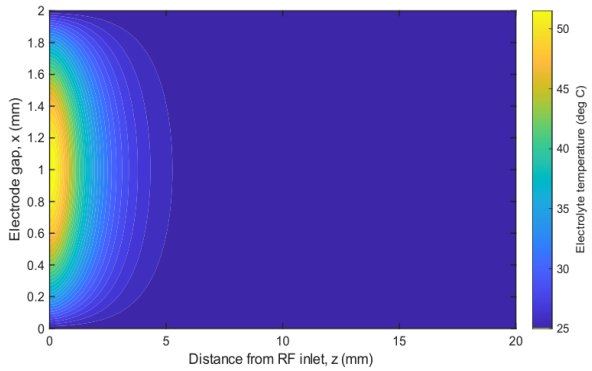

Figure 2: Existing 2D electrolyte temperature field at 3 W. The peaks occur close to the RF inlet, away from the isothermal electrode surfaces.

The calculated boundary potential and temperature fields were evaluated using Eq. (4); the resulting cathodic HER-equivalent current-density profiles are shown in Fig. 3. The maximum local cathodic current density was approximately 1182.95 A m^{-2} at the RF inlet at 3 W, compared with about 1077.09 A m^{-2} in the zero-RF case at the same location. This represents a local increase of approximately 9.83%, but integration over the electrode yields an area-averaged change of only 1.03%. The spatially resolved interpretation is therefore different from interpreting only total hydrogen output.

Because both metal faces remained at T_0, the result is not an observed 9.83% thermally accelerated HER kinetic constant. It follows from electrolyte resistance/potential redistribution within the assumed Butler–Volmer flux law. The boundary-current profiles were obtained by evaluating the prescribed interfacial current law using spatial field values. Their integrals reproduce the corresponding model-integrated electrode current to graphical accuracy.

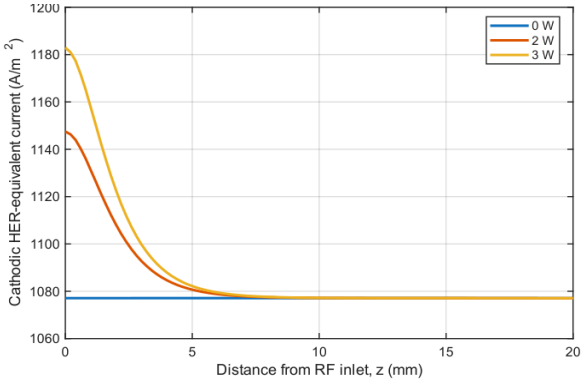

Figure 3: Calculated cathodic surface current-density distribution under zero-RF and microwave-heated conditions. Both cases share the same isothermal electrode boundary.

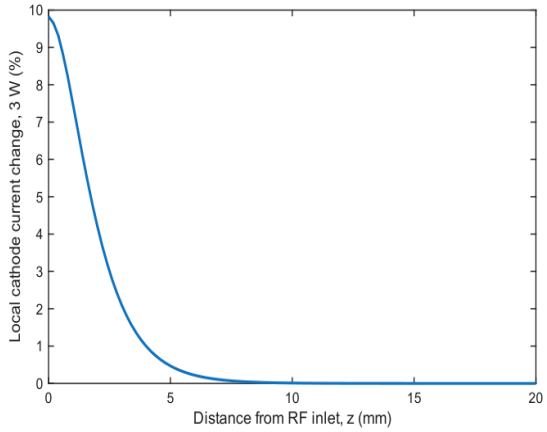

Figure 4: Local percentage change in cathodic current density at 3 W relative to the zero-RF reference at the same position. This is a model-derived spatial current redistribution, not a validated catalytic rate-enhancement measurement.

Table 2 separates spatial heating from overall energy accounting. Profile-matched heating reproduces the RF hydrogen rate, as expected from the identical imposed heat-source distribution. The mean-temperature-matched uniform heater predicts slightly higher hydrogen output, approximately 0.00463 and 0.00837 mmol h^{-1} above the microwave solutions at 2 and 3 W. These correspond to only 0.0467% and 0.0841% of the respective microwave hydrogen rates.

The extra hydrogen HHV power between 0 and 3 W was only approximately 8.05 mW, whereas the modeled microwave generator

drew an additional 4.615 W, plus a 0.0111-W rise in DC input. On this accounting basis the incremental extra hydrogen HHV output divided by extra total electrical input was approximately 0.174%. Thus a positive hydrogen-rate change does not establish favorable system energy conversion.

Table 2: Thermal-control comparisons under the same electrochemical model. Conventional heaters are idealized; the power labels denote the reference RF conditions.

Control	P (W)	$\dot{n}_{H_2}$ (mmol h^{-1})	η_{HHV} (%)	P_{ext} (W)
RF	2	9.91467	18.916	3.077
Uniform mean matched	2	9.91930	24.847	2.085
Profile matched	2	9.91467	25.518	2.000
RF	3	9.94742	13.847	4.615
Uniform mean matched	3	9.95578	18.730	3.131
Profile matched	3	9.94742	19.317	3.000

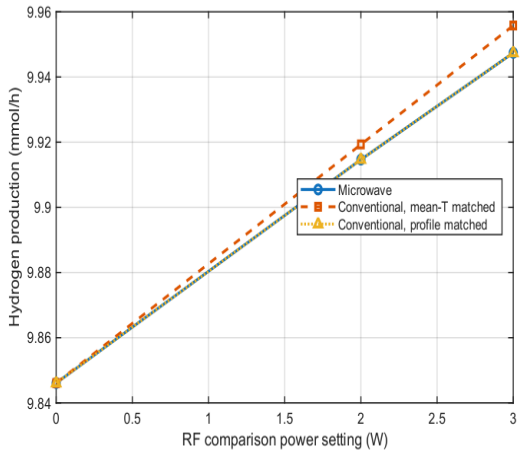

Figure 5: Reference-cell hydrogen output under microwave and two conventional-heating comparisons using the same electrochemical equations.

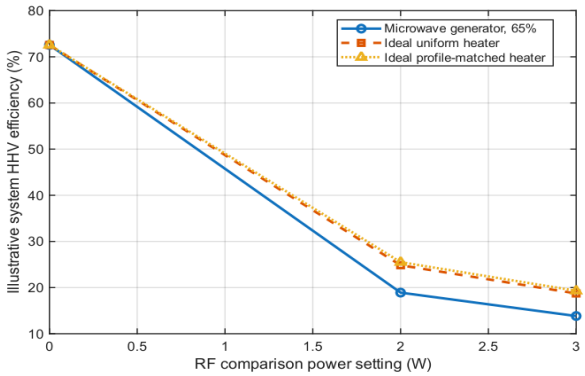

Figure 6: Illustrative system HHV efficiencies, including assumed RF-generator electrical losses. The zero-RF baseline is not an unpowered device: a 2-V DC electrode bias remains present.

The four geometrical configurations are compared in Table 3. Case B doubles absolute hydrogen output at doubled width when power is doubled, but has identical local normalized response to A in this reduced 2D model. Case D modifies source density to match A's thermal-source number while retaining different attenuation and transport groups, their hydrogen ratios are therefore similar, but not identical. Neither comparison verifies the response of an arbitrary 3D cell shape.

Table 3: Predicted RF-assisted response at the higher nominal source setting for each configuration. Configurations C and D share the same resolved two-dimensional geometry but differ in net delivered power density.

Case	Volume (cm^3)	$P_{RF,net}$ (W)	Π_{RF}	$\dot{n}_{H_2}/\dot{n}_0$
A	1.0000	3.000	0.57151	1.010291
B	2.0000	6.000	0.57151	1.010291
C	0.421875	1.265625	0.32145	1.005469
D	0.421875	2.250	0.57147	1.009557

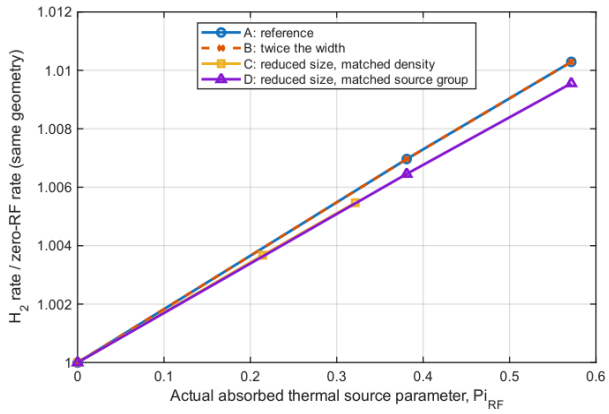

Figure 7: Normalized hydrogen response for the four modeled configurations. Matching the absorbed thermal-source parameter does not guarantee identical electrochemical behavior.

6. Paired electrochemical parameter sensitivities at zero and 2-W RF power

A one-factor-at-a-time numerical study examined KOH concentration, applied cell voltage and the nominal Butler–Volmer exchange-current densities. Each parameter setting was calculated at both zero RF and 2 W net RF inlet power, using identical meshes, geometries, electrode thermal boundary conditions and electrochemical inputs within each pair. The resulting nine pairs were checked for consistency of their numerical and physical settings before the relative hydrogen-production changes were evaluated. All 18 calculations converged and remained within the specified temperature range of the dielectric model.

Table 4: Matched-mesh, one-factor-at-a-time electrochemical sensitivity study. Baseline and RF-assisted hydrogen rates share the same geometry and numerical settings. The percentage gain compares 2 W against the corresponding zero-RF DC-biased baseline rather than against a different chemical condition. HHV values use the stipulated generator and Faradaic-efficiency assumptions.

Parameter	Setting	$\dot{n}_{H_2}$ (mmol h^{-1})		RF gain	2-W HHV
		0 W	2 W	(%)	(%)
KOH concentration	0.5 mol L^{-1}	7.027 46	7.081 08	0.763	14.597
	1.0 mol L^{-1}	9.846 09	9.914 67	0.697	18.916
	2.0 mol L^{-1}	12.76 236	12.84 180	0.622	22.750
Applied voltage	1.8 V	2.824 87	2.833 36	0.300	6.703
	2.0 V	9.846 09	9.914 67	0.697	18.916
	2.2 V	21.56 593	21.77 615	0.975	30.347
HER/OER j_0 multiplier	0.5×	6.717 37	6.754 14	0.547	14.054
	1.0×	9.846 09	9.914 67	0.697	18.916
	2.0×	13.59 156	13.70 425	0.829	23.778

At fixed 2 V, the absolute hydrogen rate increased with KOH concentration, the matched 0-W values were 7.02746, 9.84609, and 12.76236 mmol h^{-1} at 0.5, 1, and 2 mol L^{-1}, respectively. Yet the relative thermal RF-associated increment decreased from 0.763% to 0.622%, while the nominal 1 mol L^{-1} case increased by 0.697%. The concentration dependence reflects the assumed conductivity and transport closure; it is not a verified concentration optimum because the microwave dielectric properties of KOH were not experimentally calibrated.

The paired voltage sweep showed relative RF-associated gains of 0.300%, 0.697%, and 0.975% at 1.8, 2.0, and 2.2 V. In the kinetic

screen, the corresponding gains were 0.547%, 0.697%, and 0.829% when both HER/OER exchange-current densities were scaled by 0.5, 1, and 2. The latter experiment does not distinguish HER from OER sensitivity because both coefficients change simultaneously. The much larger absolute rate differences across voltage and kinetic inputs must not be mischaracterized as microwave-induced rate gains.

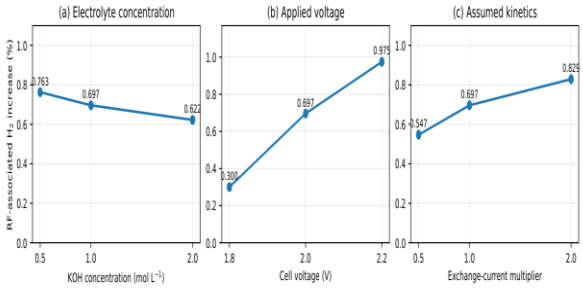

Figure 8: Relative 2-W hydrogen-production change referenced to the matched zero-RF simulation for each chemical setting.

Under the assumed fixed Faradaic efficiency, the zero-RF HHV efficiency at a fixed applied voltage depends algebraically on voltage rather than on the electrode exchange-current prefactors or KOH concentration. Thus identical zero-RF efficiencies across concentration or kinetic settings are a feature of the adopted metric, not an independently established electrochemical benefit. In every matched case, adding RF power decreases total assumed-equipment HHV efficiency markedly despite the positive hydrogen-rate increment. These paired controls isolate the within-model thermal RF association more cleanly than the prior stand-alone 2-W screens, but they cannot by themselves establish whether laboratory microwave heating differs from a realistic conventional heater. Spatially profile-matched and temperature-matched thermal controls for every parameter setting remain unavailable, as do independent electrode and dielectric calibrations.

7. New microwave-power screen and its validity threshold

A separate reference-cell power series was evaluated at 0, 0.5, 1, 2, 3, 3.5 and 4 W (Table 5). This parameter sweep employed a different spatial discretization from the reference calculations summarized in Table 1, the two sets of absolute results are therefore reported separately. At 2 W their predicted hydrogen-production rates differed by approximately 0.033%.

Table 5: Reference-cell RF-power dependence at 1 mol L^{-1} KOH and 2 V. The converged 4-W case exceeded the 333.15-K dielectric-property temperature range and is excluded from in-range quantitative interpretation.

P_{RF} (W)	T_{max} (°C)	$\dot{n}_{H_2}$ (mmol h^{-1})	η_{HHV} (%)	Screen
0	25.045	9.84925	72.579	In range
0.5	29.294	9.86680	42.378	In range
1	33.656	9.88409	29.956	In range
2	42.733	9.91791	18.921	In range
3	52.297	9.95071	13.847	In range
3.5	57.270	9.96672	12.221	In range
4	62.370	9.98249	10.938	Extrapolated

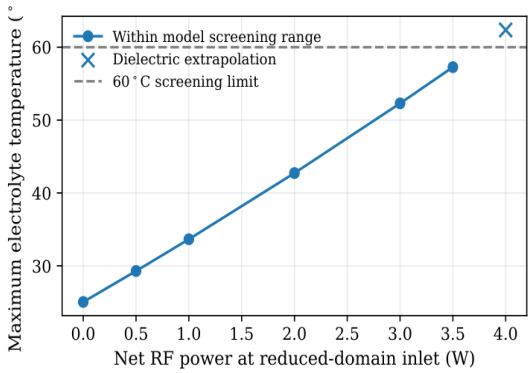

Figure 9: Maximum electrolyte temperature as a function of RF power. The 4-W point requires extrapolation of the dielectric representation; the 60°C threshold denotes its stated screening range, not a boiling limit.

The 3.5-W case remained inside the specified dielectric-temperature screening

range, with a predicted maximum temperature of 330.42 K and modeled hydrogen output 1.193% higher than the zero-RF case of the same sweep. At 4 W, the maximum was 335.52 K, above the 333.15-K interpolation ceiling. Therefore the power sweep establishes that the current model's screened numerical domain extends beyond 3 W, but does not establish the performance of a microwave-oven-powered electrolyzer. More powerful excitation would require different heat-removal conditions, independently measured KOH microwave dielectric properties, or a more complete physical description, as explained below.

8. Extension to Higher Microwave Power and Physical Limitations

There is no electromagnetic reason to select 3 W as a universal microwave-oven power ceiling. Microwave generators can supply much greater power. However, a clear distinction must be made among the microwave source output, the power coupled into the applicator and sample, and the net microwave power deposited in the electrolyte. The present 1D boundary normalization specifies the latter problem's inlet and has no realistic applicator-coupling calculation. Likewise, power density P_{abs}/V cannot by itself determine the spatial maximum of T.

A new power-sweep calculation reached 330.42 K at 3.5 W and crossed the 333.15-K solvent-relaxation screening ceiling at 4 W (335.52 K). These values were obtained directly from the reduced-model calculations rather than by extrapolating the lower-power trend. The 4-W computed hydrogen rate is explicitly flagged as dielectric-extrapolated and is not accepted as an in-range physical prediction. Stronger microwave heating can also trigger boiling, bubble-induced changes in microwave attenuation, electrode coverage, natural convection, and latent-heat

physical boiling temperature depends on pressure and composition and must not be equated automatically with 373.15 K under all KOH conditions.

To investigate a microwave oven or an industrial generator responsibly, the next model should include measured $\epsilon^*(f,T,M)$ for KOH, an actual 3D applicator including metal electrodes and coupling ports, a time-dependent heat equation with cooling/flow and electrode heat, and gas/liquid transport. A larger cell or actively cooled/flowing geometry could sustain greater total absorbed power while maintaining acceptable local temperatures, but this remains a modeling hypothesis to test. Accordingly, the power study distinguishes predictions within the specified dielectric-temperature range from numerically converged cases requiring extrapolation, the latter are not interpreted as validated physical predictions.

9. Research limitations and proposed verification

The numerical solution is internally self-consistent under its equations, but its assumed nickel kinetics, simplified OH^- replenishment, fixed Faradaic efficiency, pure-water solvent relaxation and isothermal electrodes prevent quantitative device prediction. A chemically meaningful next validation would combine nickel HER/OER polarization measurements, temperature-dependent KOH microwave dielectric spectroscopy, and independent microwave-to-heat calorimetry with fiber-optic local-temperature monitoring. At matched temperature distribution, one could then assess whether any additional microwave-related electrochemical response is detected experimentally. A high-power regime should be modeled with electrode reaction/activation heat, concentration-dependent transport, gas evolution, and eventually transient/flow coupling, without these upgrades the present generator-power efficiency comparison is a benchmark, not an optimized industrial design.

The 3-W mesh study helps bound one numerical source of uncertainty, but does not

establish kinetic-model uncertainty or systematic convergence of the heat-balance residual. Future calculations should refine the heat equation and mass balance simultaneously, confirm that cathode/anode reaction currents agree, independently audit net Poynting absorption, and report confidence intervals obtained by varying j_0, activation energies, ϵ^*, and heat-transfer assumptions. All resulting parametric values would be numerical predictions until checked against measured electrolysis cells.

10. Conclusions

Within the specified 1D RF/2D electrochemical model, localized microwave heat deposition redistributed current toward the RF inlet, but the reference 3-W case increased hydrogen production by only 1.029% and lowered illustrative system HHV efficiency to 13.85%. The local current redistribution cannot be interpreted as an intrinsic microwave effect on nickel electrocatalysis because electrode temperatures were held fixed. The spatial-profile-matched thermal control generated the same hydrogen rate by construction.

Matched-mesh zero- and 2-W chemistry comparisons showed that the relative modeled RF-associated hydrogen-rate gain fell from 0.763% to 0.622% as KOH concentration rose from 0.5 to 2 mol L^{-1}, increased from 0.300% to 0.975% across 1.8–2.2 V, and increased from 0.547% to 0.829% as both assumed exchange-current coefficients were scaled from 0.5 to 2 times nominal. These small fractional gains are distinct from the much larger changes in absolute hydrogen rate caused by changing the electrochemical input parameters. The corresponding zero-RF reference was explicitly recomputed for each case; nevertheless, the trends remain model-based thermal responses rather than validated microwave-specific catalysis. Every 2-W case had lower stipulated total-equipment HHV efficiency than its zero-RF reference. A separate power sweep remained inside the dielectric-temperature screen at 3.5 W but exceeded it at 4 W, underscoring that the 3-W threshold is a model constraint, not a microwave-generator limit. Quantitative high-power physical prediction demands measured KOH permittivity, calibrated electrode kinetics, realistic thermal management and gas–liquid transport.

References

[1] R. Pinto, M. Oliveira, and A. Borges, "An experimentally validated model of electrolyte effects in alkaline water electrolysis," *Scientific Reports* 15, 41865 (2025). doi:10.1038/s41598-025-25842-3.

[2] K. Zeng and D. Zhang, "Recent progress in alkaline water electrolysis for hydrogen production and applications," *Progress in Energy and Combustion Science* 36, 307–326 (2010). doi:10.1016/j.pecs.2009.11.002.

[3] A. Ursua, L. M. Gandia, and P. Sanchis, "Hydrogen production from water electrolysis: current status and future trends," *Proceedings of the IEEE* 100, 410–426 (2012). doi:10.1109/JPROC.2011.2156750.

[4] M. Carmo, D. L. Fritz, J. Mergel, and D. Stolten, "A comprehensive review on PEM water electrolysis," *International Journal of Hydrogen Energy* 38, 4901–4934 (2013). doi:10.1016/j.ijhydene.2013.01.151.

[5] A. Buttler and H. Spliethoff, "Current status of water electrolysis for energy storage, grid balancing and sector coupling via power-to-gas and power-to-liquids: A review," *Renewable and Sustainable Energy Reviews* 82, 2440–2454 (2018). doi:10.1016/j.rser.2017.09.003.

[6] O. Ulleberg, “Modeling of advanced alkaline electrolyzers: a system simulation approach,” *International Journal of Hydrogen Energy* 28, 21–33 (2003). doi:10.1016/S0360-3199(02)00033-2.

[7] P. M. Dieguez, A. Ursua, P. Sanchis, C. Sopena, E. Guelbenzu, and L. M. Gandia, “Thermal performance of a commercial alkaline water electrolyzer: Experimental study and mathematical modeling,” *International Journal of Hydrogen Energy* 33, 7338–7354 (2008). doi:10.1016/j.ijhydene.2008.09.051.

[8] S. Hu, B. Guo, S. Ding, F. Yang, J. Dang, B. Liu, J. Gu, J. Ma, and M. Ouyang, “A comprehensive review of alkaline water electrolysis mathematical modeling,” *Applied Energy* 327, 120099 (2022). doi:10.1016/j.apenergy.2022.120099.

[9] C. Daoudi and T. Bounahmidi, “Overview of alkaline water electrolysis modeling,” *International Journal of Hydrogen Energy* 49, 646–667 (2024). doi:10.1016/j.ijhydene.2023.08.345.

[10] A. S. Emam, M. O. Hamdan, B. A. Abu-Nabah, and E. Elnajjar, “A review on recent trends, challenges, and innovations in alkaline water electrolysis,” *International Journal of Hydrogen Energy* 64, 599–625 (2024). doi:10.1016/j.ijhydene.2024.03.238.

[11] S. Sebbahi, A. Assila, A. A. Belghiti, S. Laasri, S. Kaya, E. K. Hlil, S. Rachidi, and A. Hajjaji, “A comprehensive review of recent advances in alkaline water electrolysis for hydrogen production,” *International Journal of Hydrogen Energy* 82, 583–599 (2024). doi:10.1016/j.ijhydene.2024.07.428.

[12] M. A. Riaz, P. Trogadas, D. Ayme-Perrot, C. Sachs, N. Dubouis, H. Girault, and M.-O. Coppens, “Water electrolysis technologies: the importance of new cell designs and fundamental modelling to guide industrial-scale development,” *Energy & Environmental Science* 18, 5190–5214 (2025). doi:10.1039/D4EE05559D.

[13] A. Vedrtnam, K. Kalauni, and R. Pahwa, “A review of water electrolysis technologies with insights into optimization and numerical simulations,” *International Journal of Hydrogen Energy* 140, 694–727 (2025). doi:10.1016/j.ijhydene.2025.05.295.

[14] J. Hoffmann and B. J. M. Etzold, “Progress and perspectives on scaling next-generation alkaline water electrolysis: linking fundamentals to system design,” *Current Opinion in Chemical Engineering* 51, 101235 (2026). doi:10.1016/j.coche.2026.101235.

[15] R. J. Gilliam, J. W. Graydon, D. W. Kirk, and S. J. Thorpe, “A review of specific conductivities of potassium hydroxide solutions for various concentrations and temperatures,” *International Journal of Hydrogen Energy* 32, 359–364 (2007). doi:10.1016/j.ijhydene.2006.10.062.

[16] U. Kaatze, “Complex permittivity of water as a function of frequency and temperature,” *Journal of Chemical & Engineering Data* 34, 371–374 (1989). doi:10.1021/je00058a001.

[17] W. J. Ellison, “Permittivity of pure water, at standard atmospheric pressure, over the frequency range 0–25 THz and the temperature range 0–100 degrees C,” *Journal of Physical and Chemical Reference Data* 36, 1–18 (2007). doi:10.1063/1.2360986.

[18] K. E. Mattar and H. A. Buckmaster, “25 degrees C complex permittivity of water from 65 to 75 GHz,” *Journal of Physics D: Applied Physics* 23, 1464 (1990). doi:10.1088/0022-3727/23/11/018.

[19] H. Tuysuz, “Alkaline water electrolysis for green hydrogen production,” *Accounts of Chemical Research* 57, 558–567 (2024). doi:10.1021/acs.accounts.3c00709.

[20] N. Wang, S. Song, W. Wu, Z. Deng, and C. Tang, “Bridging laboratory electrocatalysts with industrially relevant alkaline water electrolyzers,” *Advanced Energy Materials* 14, 2303451 (2024). doi:10.1002/aenm.202303451.

[21] Z. Zou, K. Dastafkan, Y. Shao, C. Zhao, and Q. Wang, “Electrocatalysts for alkaline water electrolysis at ampere-level current densities: A review,” *International Journal of Hydrogen Energy* 51, 667–684 (2024). doi:10.1016/j.ijhydene.2023.07.026.

[22] I. M. Perovic, S. D. Mitrovic, S. M. Brkovic, and I. A. Pasti, “Advances in nickel-based catalysts for alkaline water electrolysis: Comprehensive review of current research direction for HER and OER applications,” *The Chemical Record* 25, e202500049 (2025). doi:10.1002/tcr.202500049.

[23] S. D. Mitrovic, I. M. Perovic, S. M. Brkovic, M. Seovic, P. Lausevic, and I. A. Pasti, “The electrolyte effects on the kinetics of hydrogen and oxygen evolution reaction on polycrystalline nickel in alkaline media,” *International Journal of Hydrogen Energy* 177, 151605 (2025). doi:10.1016/j.ijhydene.2025.151605.

[24] W. Y. Noh, S. J. Kazmouz, S. Lee, J.-K. Peng, T. J. Shin, and M. Shviro, “Decoupling electrode kinetics to elucidate reaction mechanisms in alkaline water electrolysis,” *Energy & Environmental Science* 18, 8679–8696 (2025). doi:10.1039/D5EE03044G.

[25] N. Esfandiari, M. Aliofkhazraei, A. N. Colli, F. C. Walsh, S. Cherevko, L. A. Kibler, M. M. Elnagar, P. D. Lund, D. Zhang, S. Omanovic, and J. Lee, “Metal-based cathodes for hydrogen production by alkaline water electrolysis: Review of materials, degradation mechanism, and durability tests,” *Progress in Materials Science* 144, 101254 (2024). doi:10.1016/j.pmatsci.2024.101254.

[26] J. Li, Y. Ma, X. Mu, X. Wang, Y. Li, H. Ma, and Z. Guo, “Recent advances and perspectives on coupled water electrolysis for energy-saving hydrogen production,” *Advanced Science* 12, e2411964 (2025). doi:10.1002/advs.202411964.

[27] M. Aligholivand, Z. Shaghaghi, R. Bikas, and A. Kozakiewicz, “Electrocatalytic water oxidation by a Ni(II) salophen-type complex,” *RSC Advances* **9**, 40424–40436 (2019). doi:10.1039/C9RA08585H.

[28] Z. Shaghaghi, M. Aligholivand, and R. Mohammad-Rezaei, “Enhanced water splitting through different substituted cobalt-salophen electrocatalysts,” *International Journal of Hydrogen Energy* **46**, 389–402 (2021). doi:10.1016/j.ijhydene.2020.09.162.

[29] Z. Shaghaghi, R. Mohammad-Rezaei, and S. Jafari, “Efficient electrochemical water oxidation mediated by different substituted manganese-salophen complexes,” *Journal of Electroanalytical Chemistry*, vol. 922, art. no. 116733 (2022). doi:10.1016/j.jelechem.2022.116733.

[30] S. Jafari and Z. Shaghaghi, "CeO_2/CuO/NiO hybrid nanostructures loaded on N-doped reduced graphene oxide nanosheets as an efficient electrocatalyst for water oxidation and non-enzymatic glucose detection," *Dalton Transactions* **52**, 7564–7580 (2023). doi:10.1039/D3DT00527E.

[31] Z. Shaghaghi and S. Akbari, "Hydrogen and oxygen production on Ag_2O/NiO hybrid nanostructures via electrochemical water splitting," *International Journal of Hydrogen Energy* **51**, 936–949 (2024). doi:10.1016/j.ijhydene.2023.09.066.

[32] J. Lee, A. Alam, C. Park, S. Yoon, and H. Ju, "Modeling of gas evolution processes in porous electrodes of zero-gap alkaline water electrolysis cells," *Fuel* 315, 123273 (2022). doi:10.1016/j.fuel.2022.123273.

[33] F. Khalighi, N. G. Deen, Y. Tang, and A. W. Vreman, "Hydrogen bubble growth in alkaline water electrolysis: An immersed boundary simulation study," *Chemical Engineering Science* 267, 118280 (2023). doi:10.1016/j.ces.2022.118280.

[34] F. Rocha, R. Delmelle, C. Georgiadis, and J. Proost, "Electrochemical performance enhancement of 3D printed electrodes tailored for enhanced gas evacuation during alkaline water electrolysis," *Advanced Energy Materials* 13, 2203087 (2023). doi:10.1002/aenm.202203087.

[35] M.-A. Babay, M. Adar, A. Chebak, and M. Mabrouki, "Dynamics of gas generation in porous electrode alkaline electrolysis cells: An investigation and optimization using machine learning," *Energies* 16, 5365 (2023). doi:10.3390/en16145365.

[36] H. Qiu, K. Obata, Z. Yuan, T. Nishimoto, Y. Lee, K. Nagato, I. Kinefuchi, J. Shiomi, and K. Takanabe, "Quantitative description of bubble formation in response to electrolyte engineering," *Langmuir* 39, 4993–5001 (2023). doi:10.1021/acs.langmuir.2c03488.

[37] H. Qiu, K. Obata, K. Tsuburaya, T. Nishimoto, K. Nagato, and K. Takanabe, "Impact of gas bubble slug on high-frequency resistance and cell voltage in water electrolysis device," *Journal of Power Sources* 611, 234765 (2024). doi:10.1016/j.jpowsour.2024.234765.

[38] J. M. Serra, J. F. Borras-Morell, B. Garcia-Banos, M. Balaguer, P. Plaza-Gonzalez, J. Santos-Blasco, D. Catalan-Martinez, L. Navarrete, and J. M. Catala-Civera, "Hydrogen production via microwave-induced water splitting at low temperature," *Nature Energy* 5, 910–919 (2020). doi:10.1038/s41560-020-00720-6.

[39] A. Dominguez-Saldana, L. Navarrete, M. Balaguer, A. J. Carrillo, J. Santos, B. Garcia-Banos, P. Plaza-Gonzalez, D. Catalan-Martinez, J. M. Catala-Civera, and J. M. Serra, "Enhanced hydrogen production in microwave-driven water-splitting redox cycles by engineering ceria properties," *Advanced Energy Materials* 14, 2401443 (2024). doi:10.1002/aenm.202401443.

[40] D. Erdemir and I. Dincer, "Cleaner hydrogen production by microwaves: Experimental investigation and comparative assessment," *Journal of Cleaner Production* 509, 145602 (2025). doi:10.1016/j.jclepro.2025.145602.

[41] Q. Zhao, P. Zhou, and X. Zhao, “Challenges and opportunities of microwave technology in hydrogen production, storage and utilization: A review,” *International Journal of Hydrogen Energy* 134, 283–298 (2025). doi:10.1016/j.ijhydene.2025.04.505.

[42] D. R. Stanisavljev, T. D. Grozdić, M. P. Marčeta Kaninski, A. R. Djordjević, and D. Lj. Stojić, “The microwave influence on the electrolytic decomposition of KOH water solution,” *Electrochemistry Communications* **9**, 901–904 (2007). doi:10.1016/j.elecom.2006.12.004.

[43] National Research Council, *Microwave Processing of Materials*, The National Academies Press, Washington, DC (1994). https://doi.org/10.17226/2266.

[44] U.S. Department of Energy, *Saving Energy with Electric Resistance Heating*, National Renewable Energy Laboratory, Report No. DOE/GO-10097-381, NREL/BR-330-6987 (1997). https://www.nre

l.gov/docs/legosti/fy97/6987.pdf.